

Appendix A

Chapter 2 Supplementary Figures

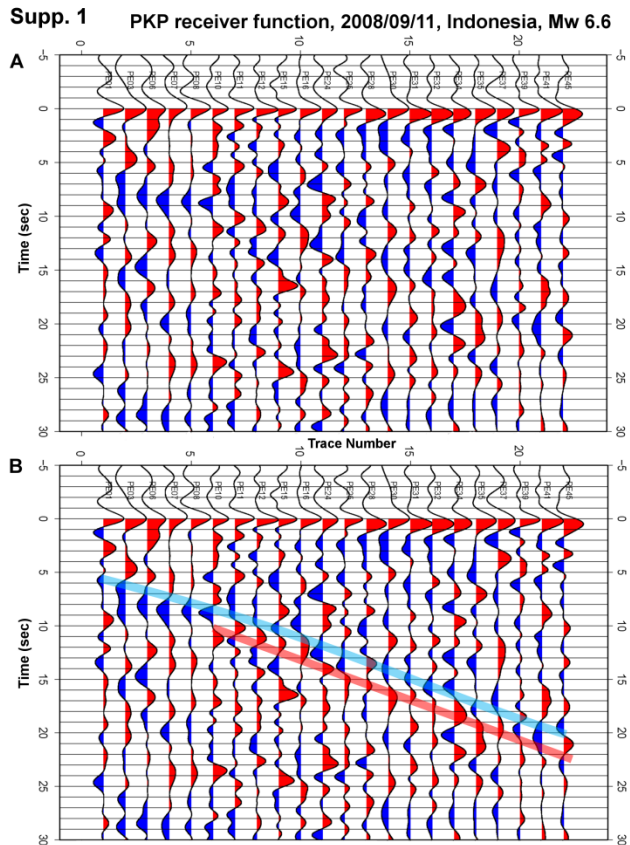


Figure A.1: Figures 2.4 and 2.9 show examples of PKP data and a PKP backprojected receiver function image. The example above shows individual PKP receiver functions. A) Example of PKP receiver functions from a magnitude 6.6 earthquake near Indonesia occurring on 2008/09/11. B): Shows an interpretation of the above image with the approximate location of the signal from the slab. The negative signal (highlighted in blue) represents the top of the oceanic crust and the positive pulses (highlighted in red) represent the bottom of the oceanic crust.

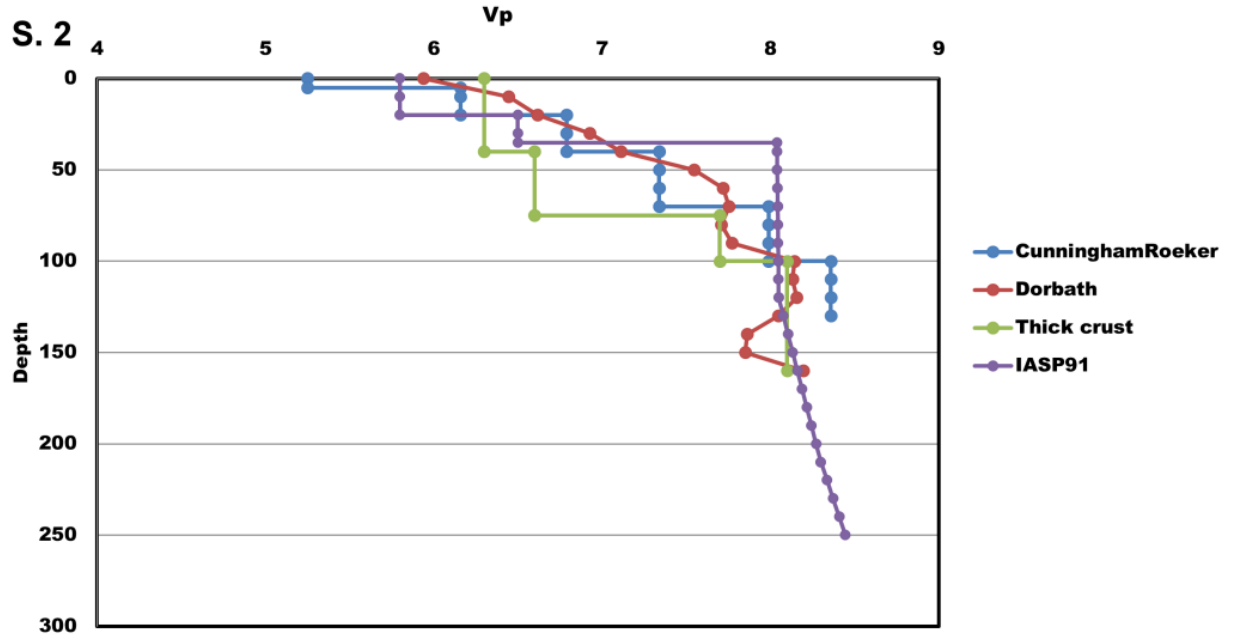


Figure A.2: P wave velocity models considered in this study. Models from Cunningham and Roecker (1986) and Dorbath et al (2008) are shown along with the IASP91 model and a simplified model for thickened crust.

References

- Cunningham, P., and S. Roecker (1986), Three-dimensional P and S Wave Velocity Structures of Southern Peru and Their Tectonic Implications, *J. of Geophys. Res.*, 91 (B9), 9517–9532.
- Dorbath, C., M. Gerbault, G. Carrier, and M. Guiraud (2008), Double seismic zone of the Nazca plate in Northern Chile: High-resolution velocity structure, petrological implications, and thermomechanical modeling, *Geochem., Geophys., Geosys.*, 9 (7), Q07, 2006.

Supp. 3

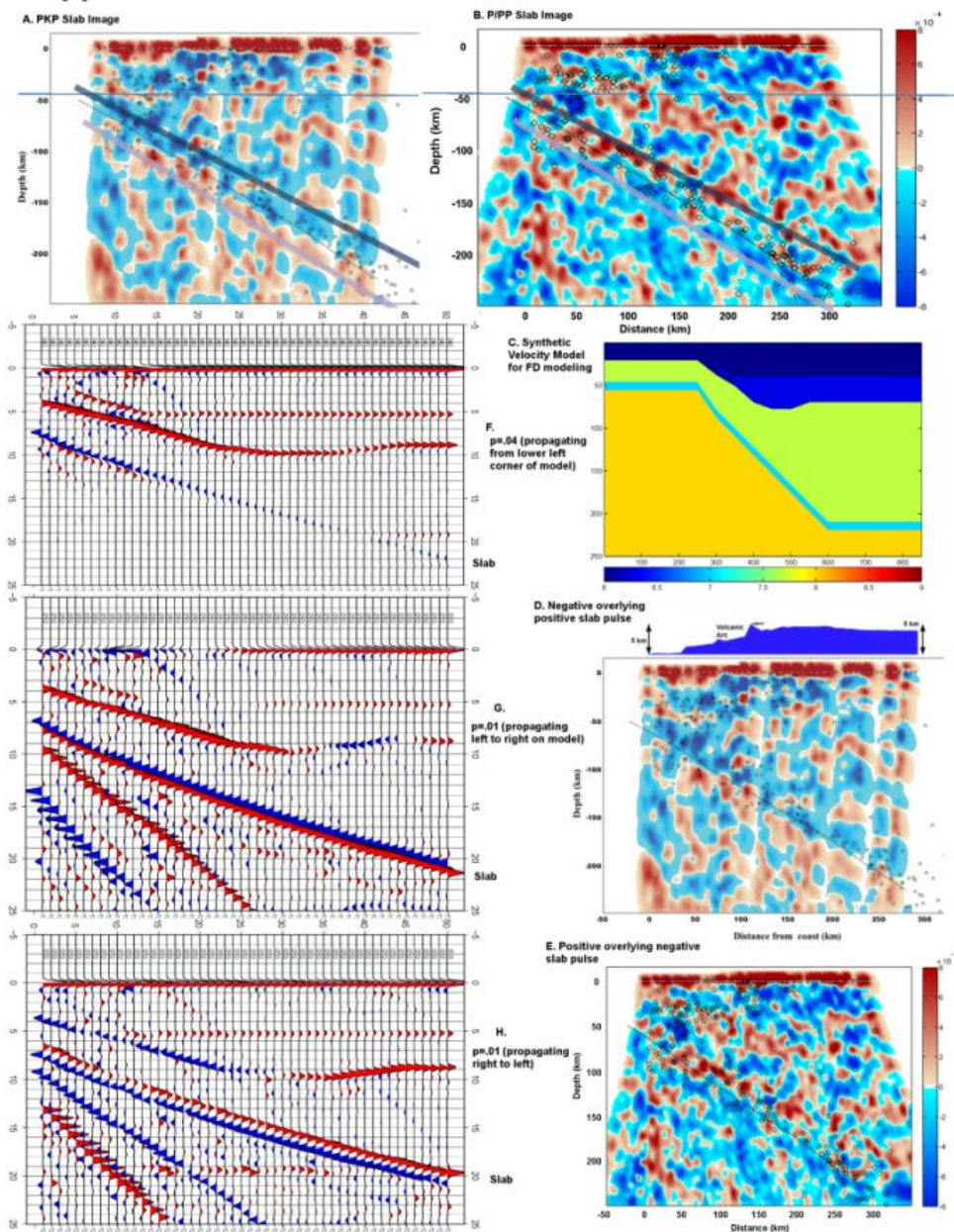


Figure A.3: Analysis of differences between observed slab between PKP image (A) and P/PP image (B). There appears to be an inversion where the PKP image has a negative pulse overlying a positive pulse and the P/PP image has a positive pulse overlying a negative pulse. The dip angle for subducting Nazca plate does not change. C) P wave velocity model used to produce finite difference synthetics. D and E) Calculations using the Zoeppritz equation for transmission coefficients using values from the model in C for an incident wave going from the mantle to the oceanic crust and from the oceanic crust to the mantle wedge as a function of angle. Note in (D) that there is a phase angle inversion

for high angles of incidence. F) Model for a standard teleseismic wave with ray parameter 0.04. G and H) Waves with ray parameters of 0.01 (similar to PKP waves) coming from difference directions. Note that depending on orientation it is possible to have either a negative pulse overlaying a positive or positive overlaying a negative pulse. The direction and angle of incidence are suggested as possible factors in the sign inversion for the slab observed in the receiver function images.

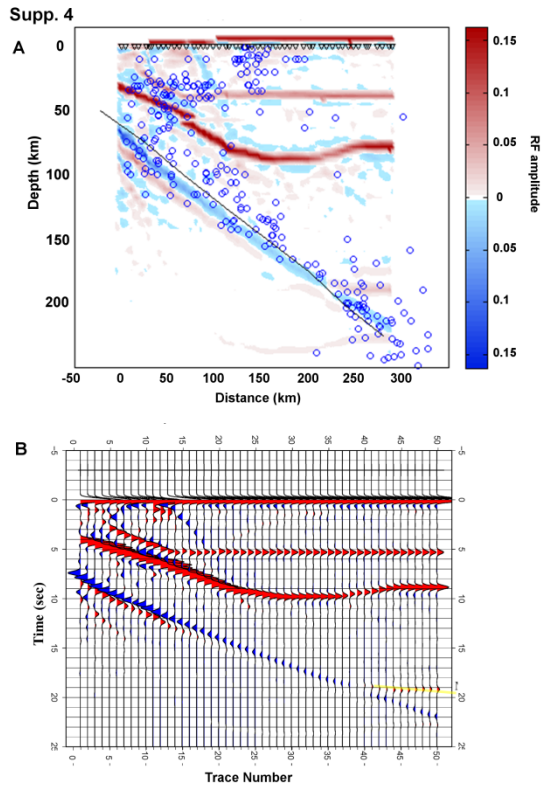


Figure A.4: Receiver function image of the synthetics from Figure 10B showing all results as a function of depth.

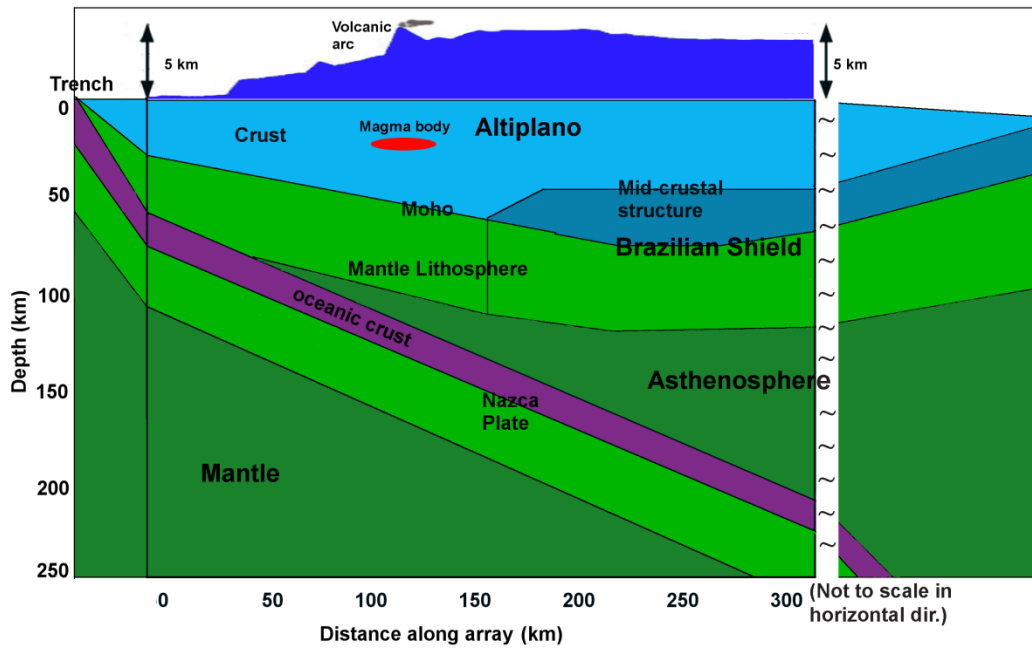


Figure A.5: More detailed cartoon of Line 1 based on Figure 2.16 which shows the trench, crust and mantle lithosphere, Brazilian Shield, and Nazca plate. Depths are approximate.

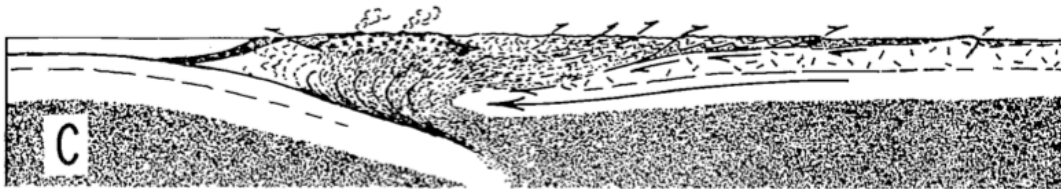


Fig. 131. — Trois schémas de tectonique des plaques susceptibles de rendre compte de la tectonique en compression dans une chaîne « cordillère »: A. inspiré de X. LE PICHON (1968), B. inspiré de B. P. LUYENDICK (1970), C. d'après P. J. CONEY (1970)

Figure A.26 The underthrusting of the Brazilian Shield was first suggested by Megard (1978). A figure from his book is shown above. Compare with model in figure A.5.

Reference:

• Megard F.. Etudes géologiques des Andes du Perou Central. Book (1978) pp. 1-315.

Appendix B

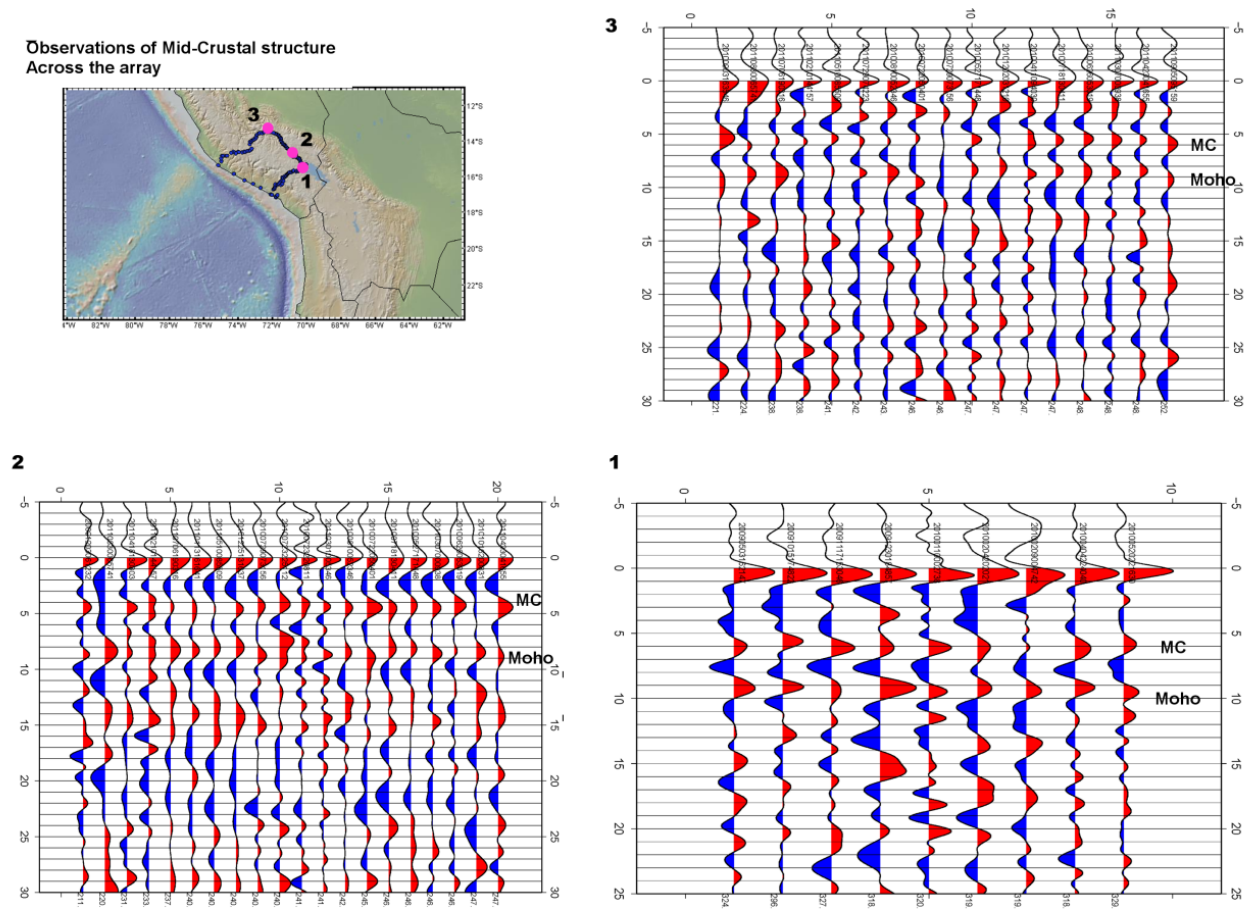
Observations of Mid-Crustal structure
Across the array

Figure B.1. Sample receiver functions showing observations of a midcrustal structure at various points of the array. Each example shows multiple events for a single station shown on the map as a pink circle. The midcrustal structure at around 5 seconds (~40 km depth) is denoted as MC and the signal from the Moho is also shown.

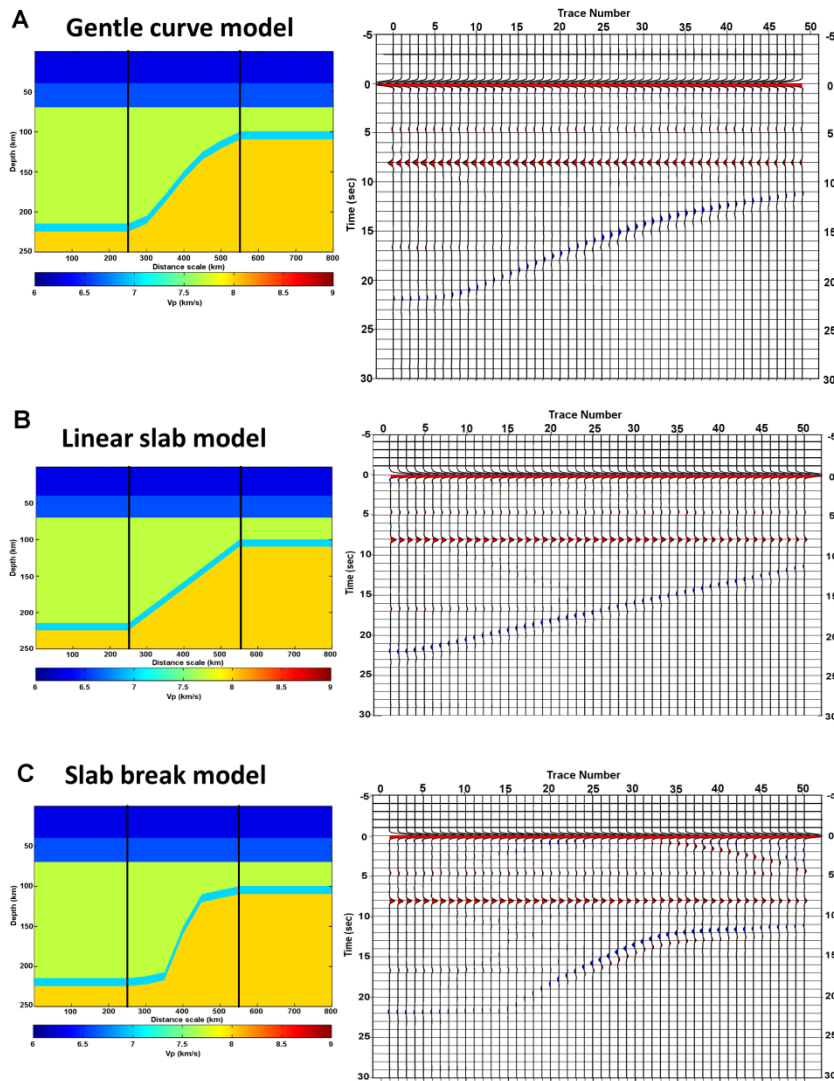


Figure B.2. Different models for Line 2, the transition from steep to shallow subduction. Three models were tested with finite difference modeling to produce synthetic receiver functions (see figure 3.3 for model used for Line 2). (A) Gently curving model comparable to figure 3.3 and resultant synthetics, (B) linear slab model and synthetics, (C) step transition from normal to flat slab subduction (as might be seen if there was a slab break) and corresponding synthetics.

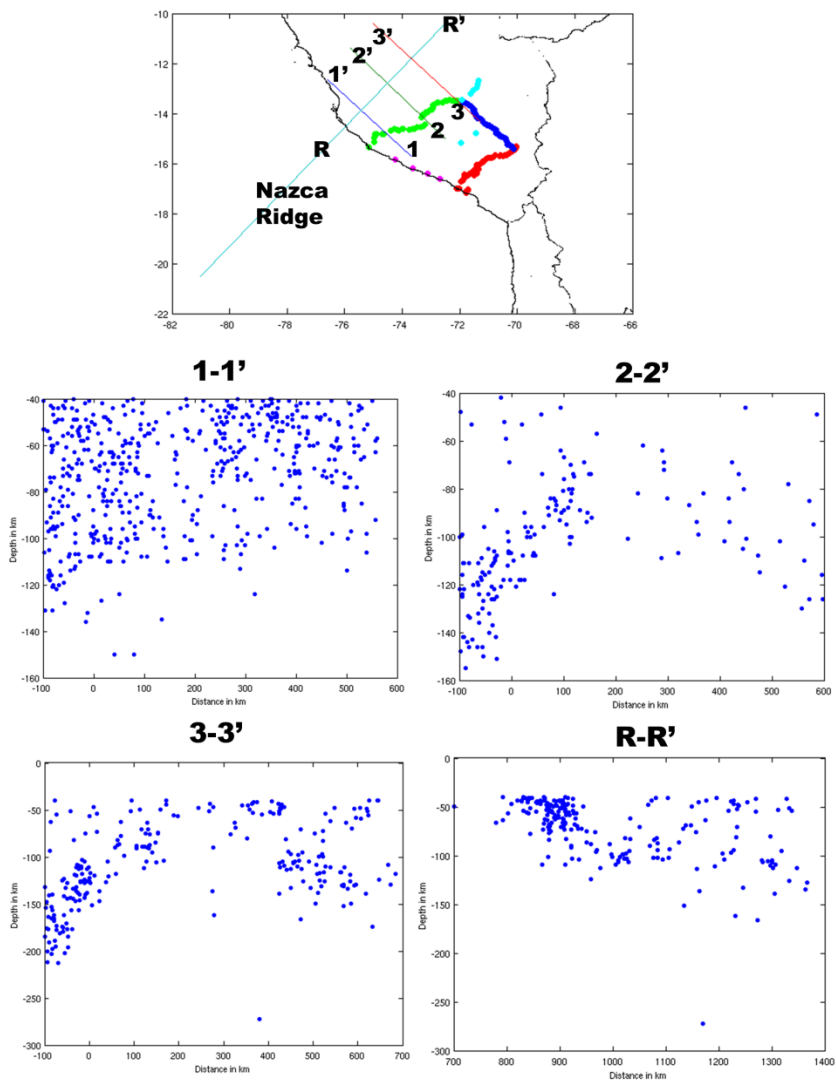
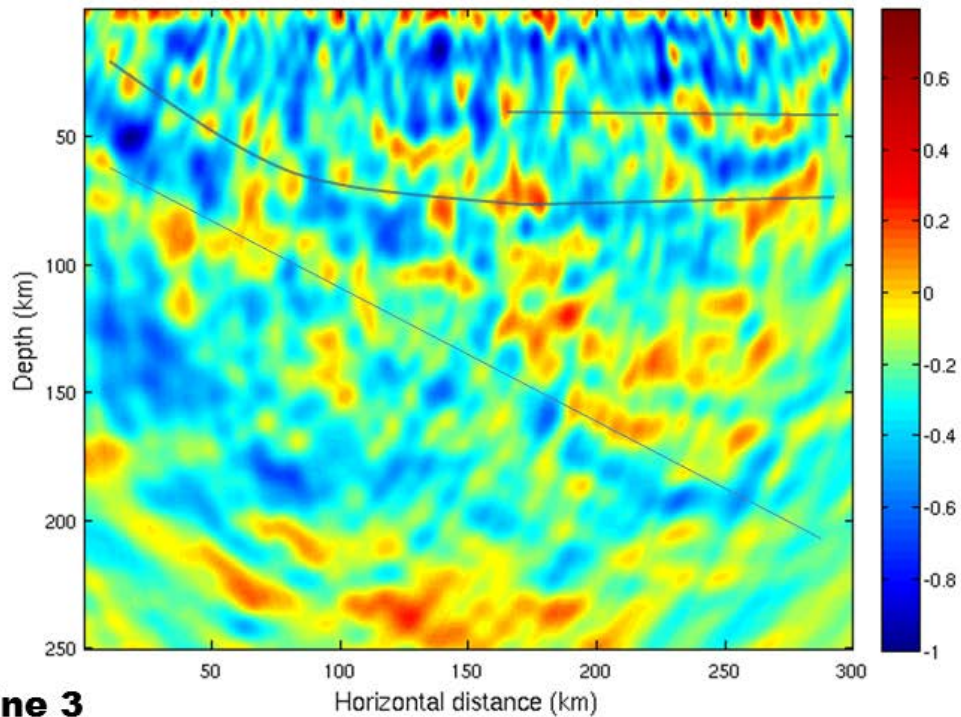
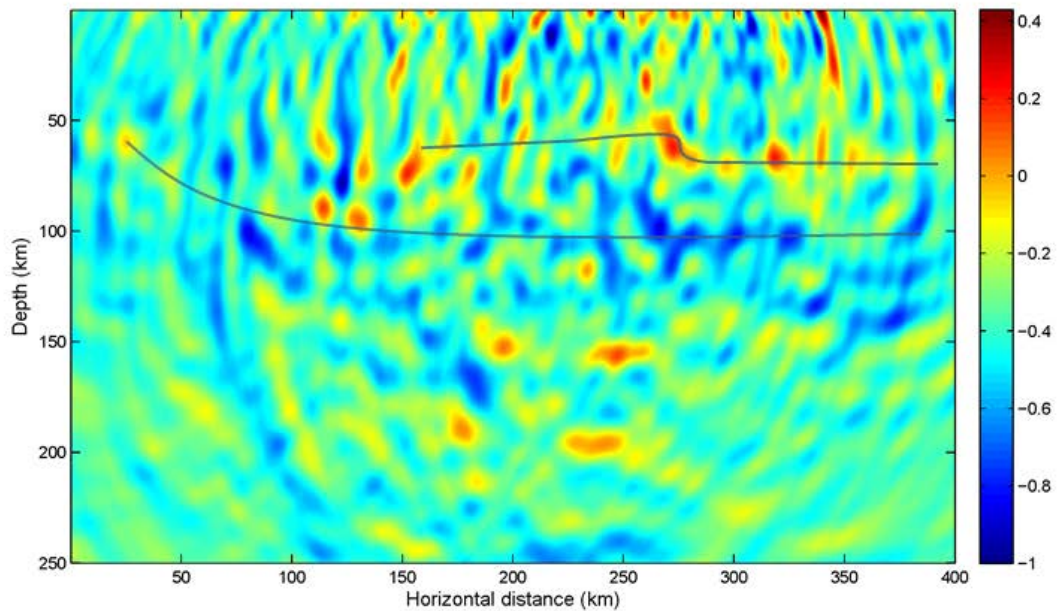
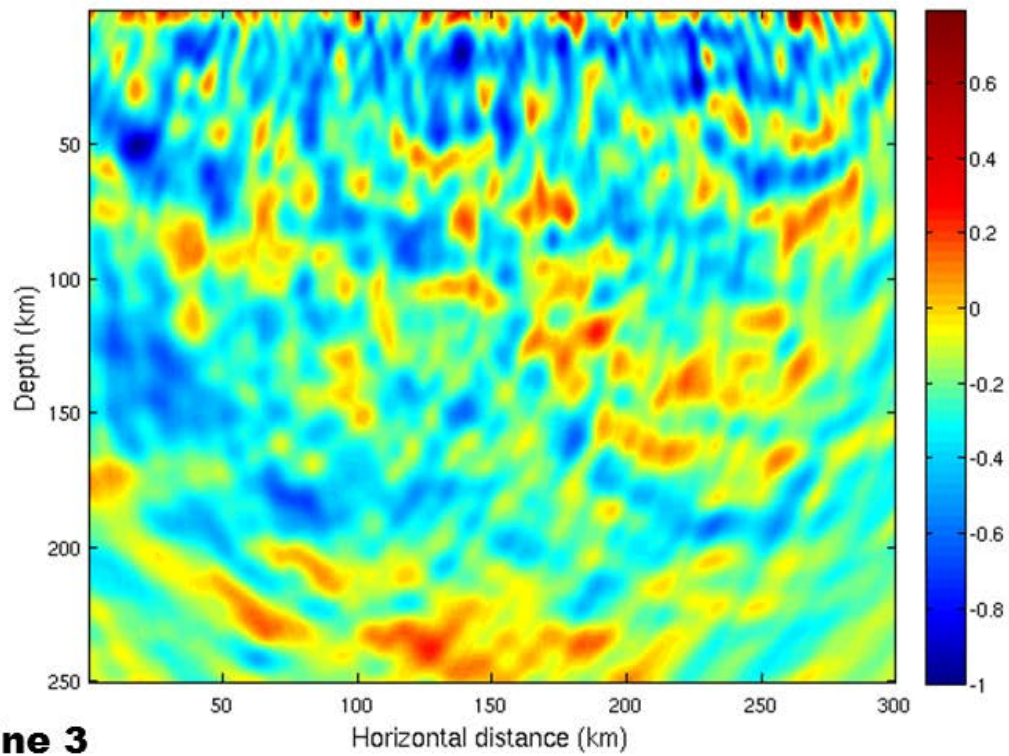
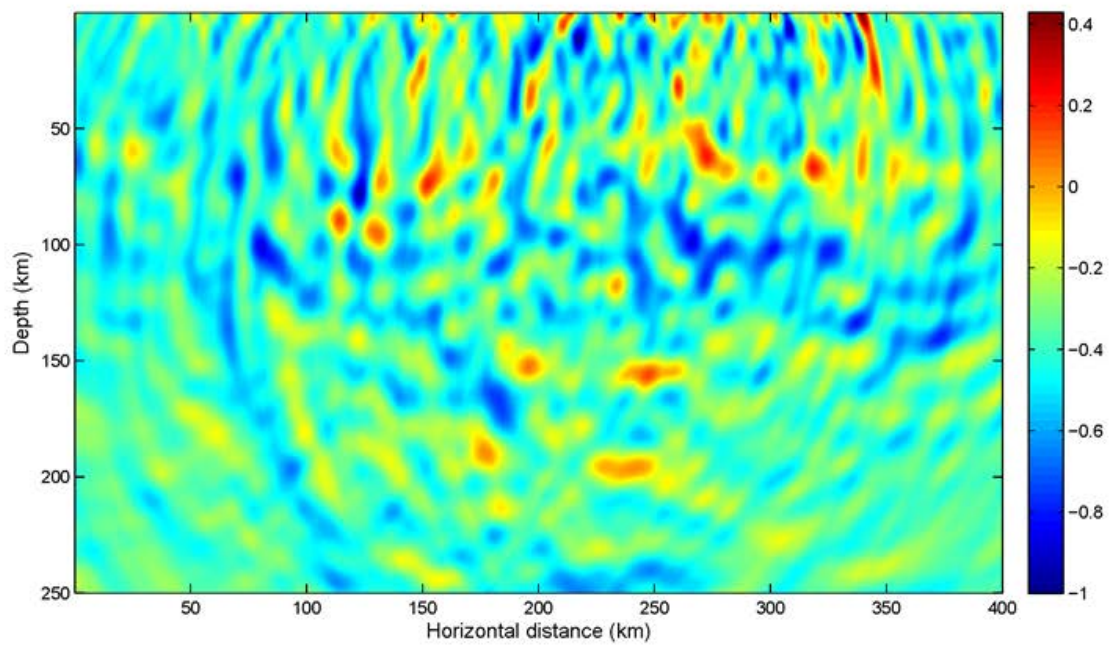


Figure B.3. Seismicity cross sections across the Nazca Ridge. Three cross sections (1-1', 2-2', and 3-3') are shown on the map. The fourth cross section (R-R') is along the trend of the ridge. Locations are from the NEIC catalog for earthquakes greater than magnitude 4 with depths greater than 40 km to avoid much of the crustal seismicity. The first cross section (1-1') closest to the coast, contains the most seismicity distributed almost evenly throughout the upper 100km. There appears to be a slight

lessening of seismicity at all depths at a distance of about 120-150km along the profile which is the approximate location of the Nazca Ridge. Profiles 2-2' and 3-3' both show a change in the seismicity from deep to shallow starting at the southernmost points of the profiles and ending at the Nazca Ridge. This is followed by a lessening of seismicity at the Ridge and slightly deeper seismicity (100-130km depth) in the flat slab region further north. The profile along the ridge shows shallow crustal seismicity near the trench and deepening to 100-120km further to the north. Other seismic catalogs were also considered (Engdahl and IGP locations) but had significantly fewer events than NEIC to recognize trends. Relocation of the events will lessen the uncertainty in depths

Line 1**Line 3**

B.4. Migrated images of Lines 1 and 3 (Compare to migrated image of Line 2 in figure 2.5). Lines of been added to show approximate locations of structures such as slab, Moho, and mid-crustal structure.

Line 1**Line 3**

B.5 Migrated images of Lines 1 and 3 as in figure B.4 but without any interpretive lines.

Appendix C

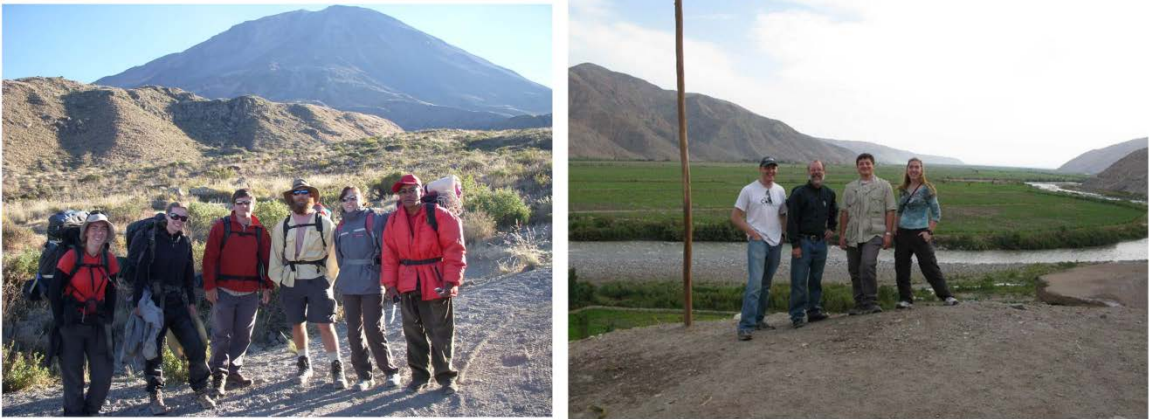


Figure C.1 Photos of participants in the installation of broadband seismic equipment in Peru. Photo on the left (listed from left to right): Kristin Phillips, Emily Foote, Igor Stubailo, Steven Skinner, Jennifer Sery, and Victor Aguilar. Photo on the right: Allan Husker, Richard Guy, Igor Stubailo, and Kristin Phillips.



Figure C.2 Photos showing the process of wirelessly connecting stations for Line 1 using Yagis and parabolic antennas. Sites had to be carefully selected so that they could obtain a good signal from neighboring stations.

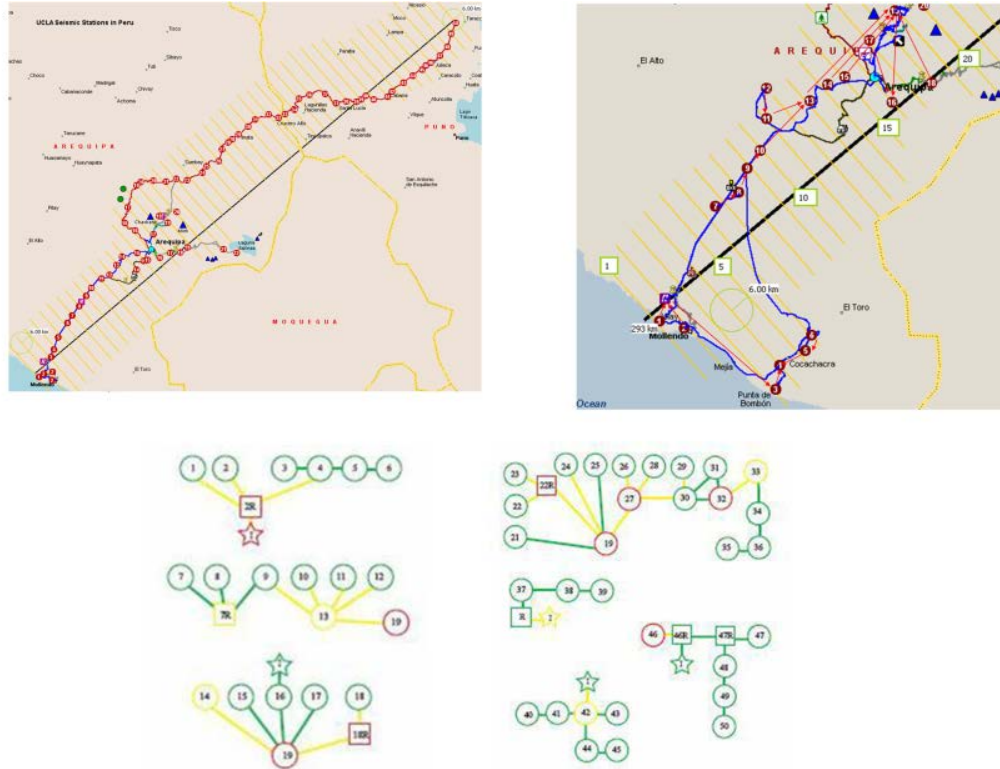


Figure C.3 Maps of the wireless connections for Line 1. The top maps show the connections in map view while the bottom figures show a link map of how all the stations are connected. Stars are locations with internet access, squares show relay sites which were put in place to help relay the signal and may not have any equipment installed, and regular sites are circles. Colors are indicative of the state of readiness of the sites at the time the link map was created (green for complete, yellow for partially complete, and red for not yet existing)



Figure C.4 Photos showing site preparation procedure for the installation of broadband stations which included digging holes for the sensor and box, installing masts for antennas and solar panels, obtaining electrical connectivity, and moving equipment.



Figure C.5 Photos show a few field challenges such as water filling boxes and holes, solar panels not generating sufficient power, and equipment which gets damaged, malfunctions, or is stolen.

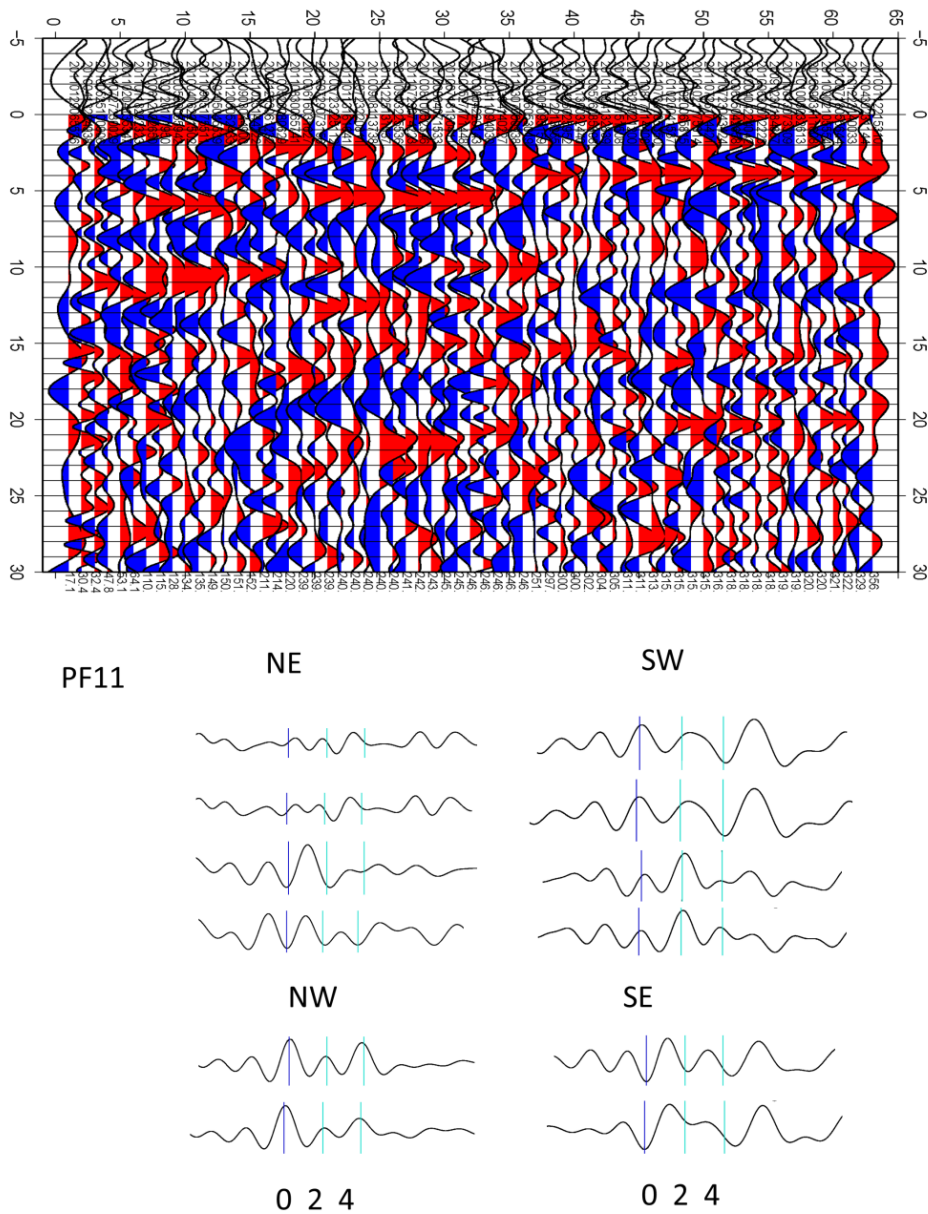


Figure C.6 Transverse receiver functions for station PF11 (Line 2) and comparison of stacks from the major azimuthal directions. Comparing the NE and SW directions, and the NW to the SE directions shows that at the times marked, the stacks from 180 degrees apart have roughly opposite polarities which may be indicative of anisotropy.

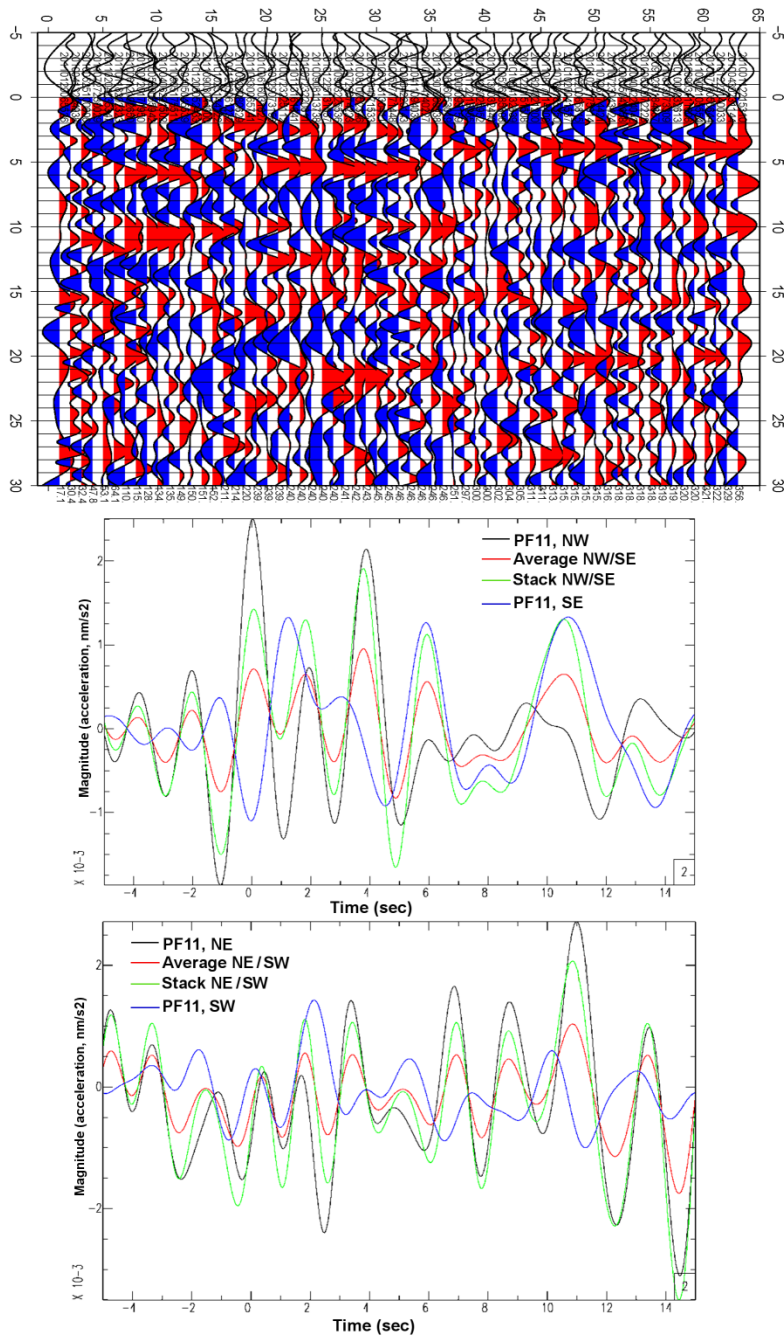


Figure C.7 Transverse receiver functions as in station PF11 (Line 2) but here showing the traces from the different directions along with their stacks and the average of the two traces.

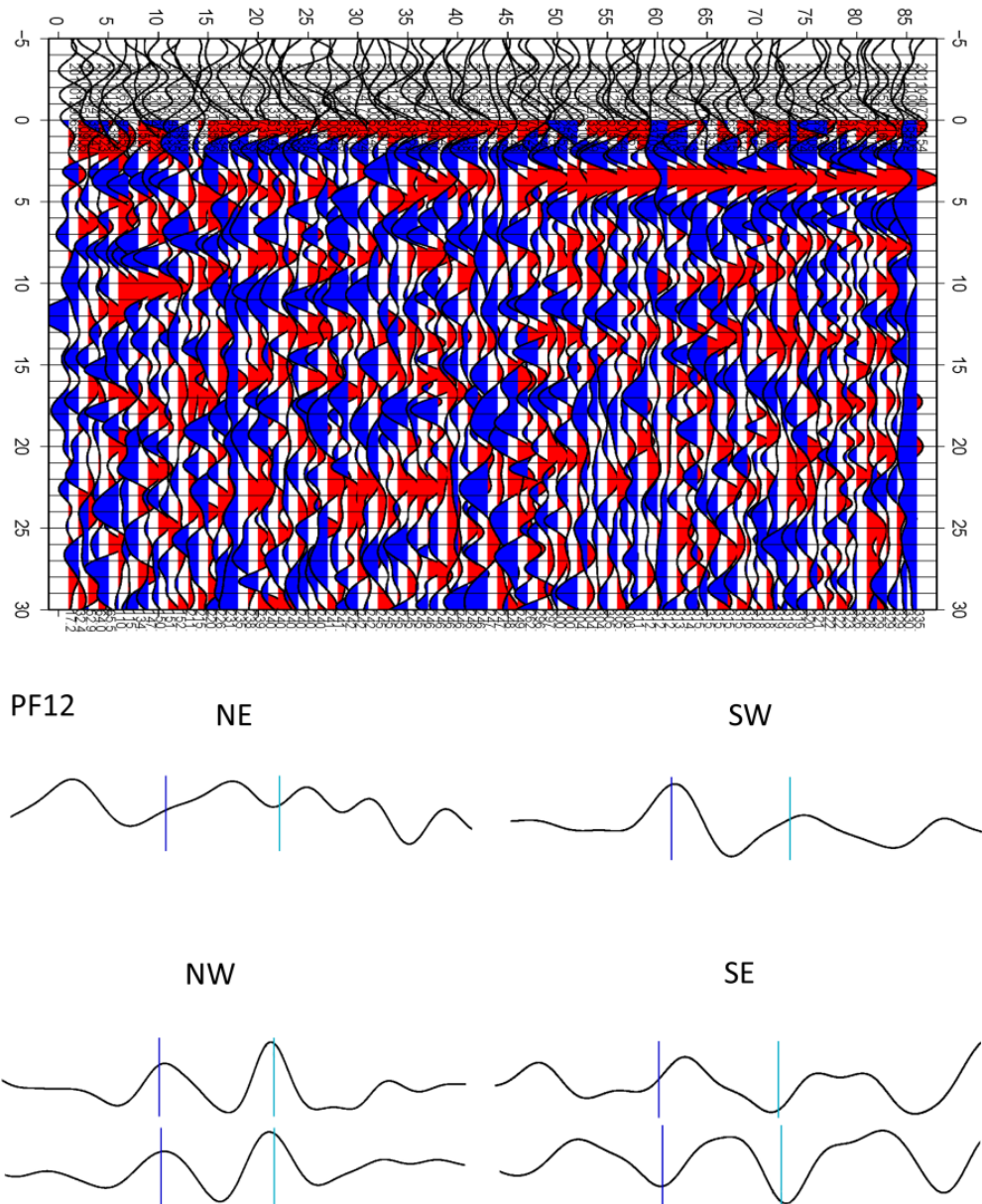


Figure C.8 Transverse receiver functions and directional stacks for station PF12 (Line 2).

Note the polarity differences between NE and SW directions and between the NW and SE directions.

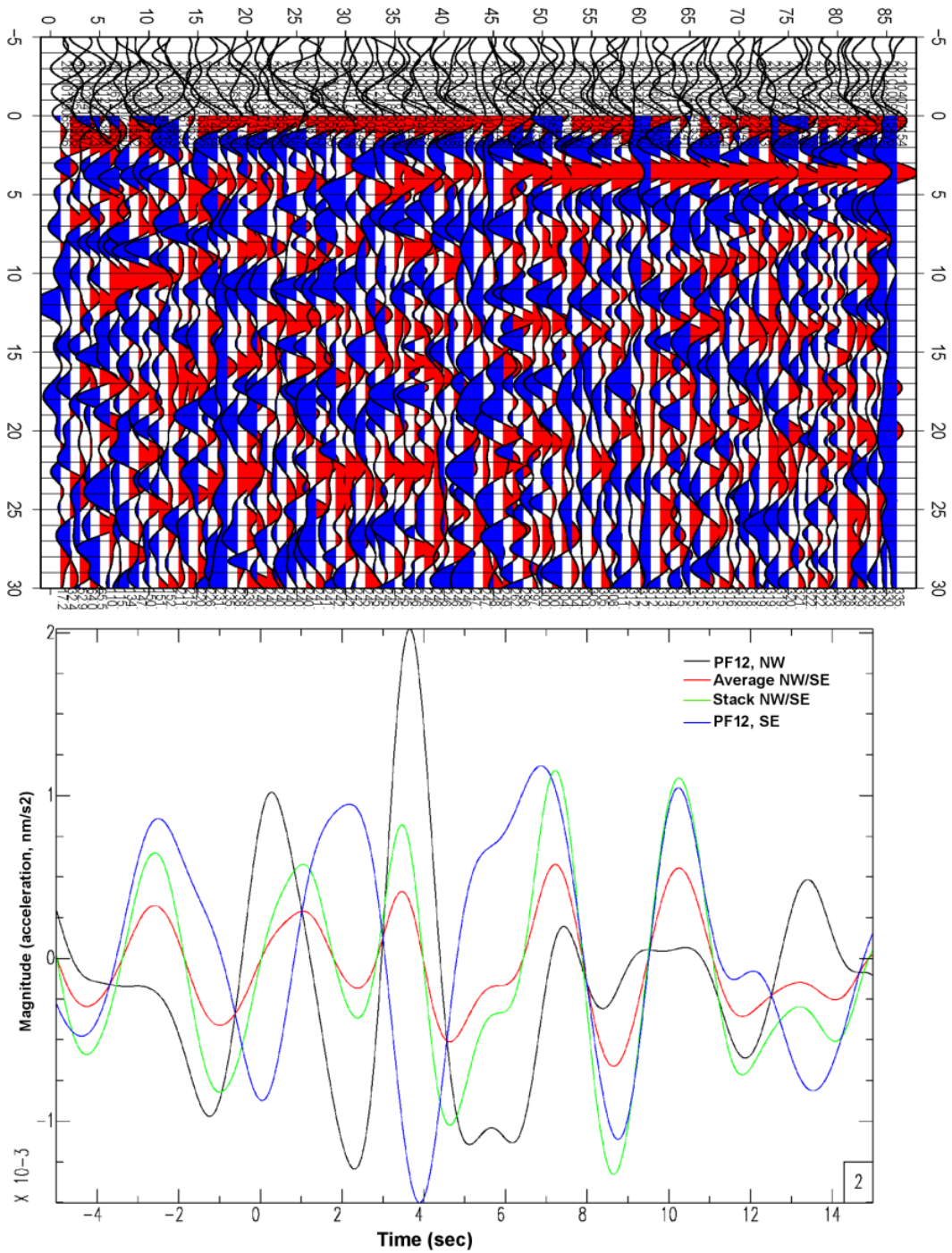


Figure C.9 Transverse RFs for station PF12 as in Figure C.8 but showing the NW and SE traces on the same scale with their stack and the average of the two.

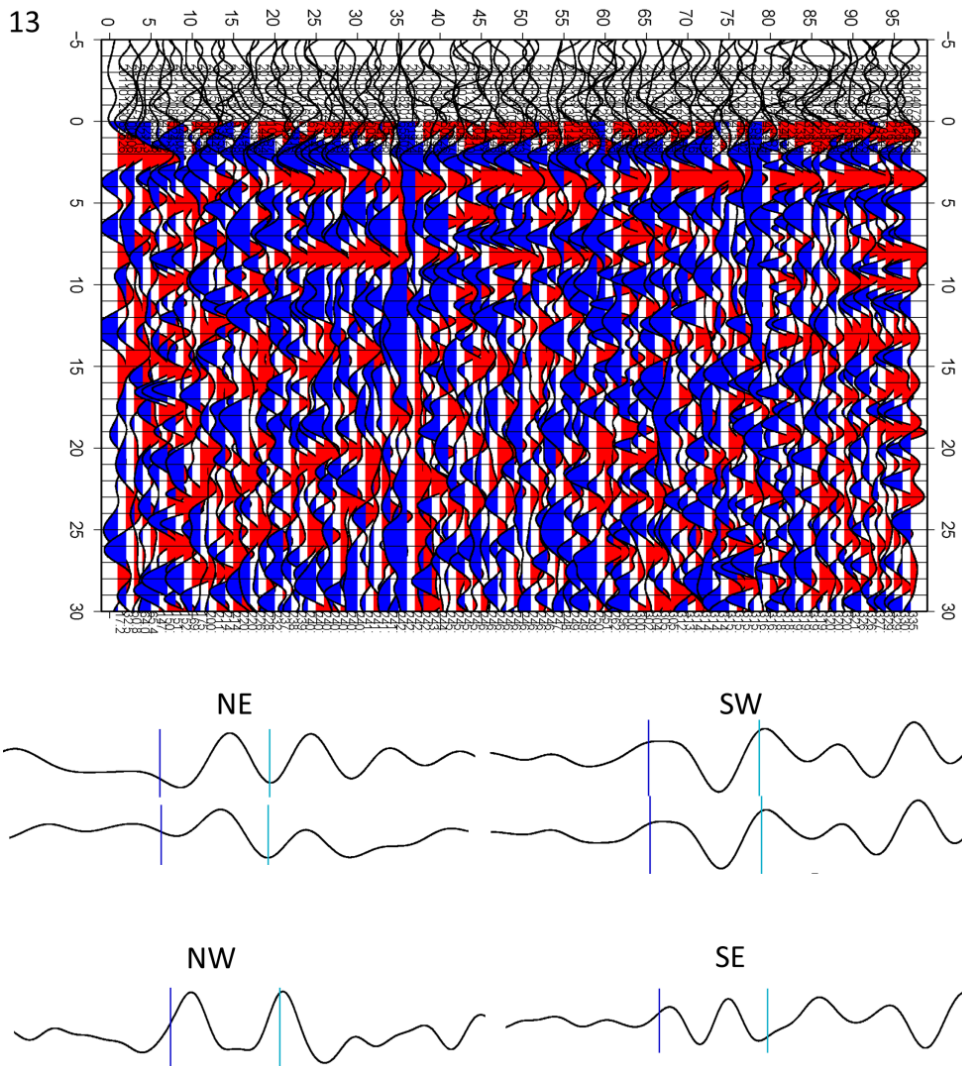


Figure C.10 Transverse RFs for PF13 (Line 2) and stacks from the major azimuthal directions. Note the polarity differences. However for the NW/SE directions, the arrival at time equals zero is of the same polarity although the second marked arrival is of opposite polarities.

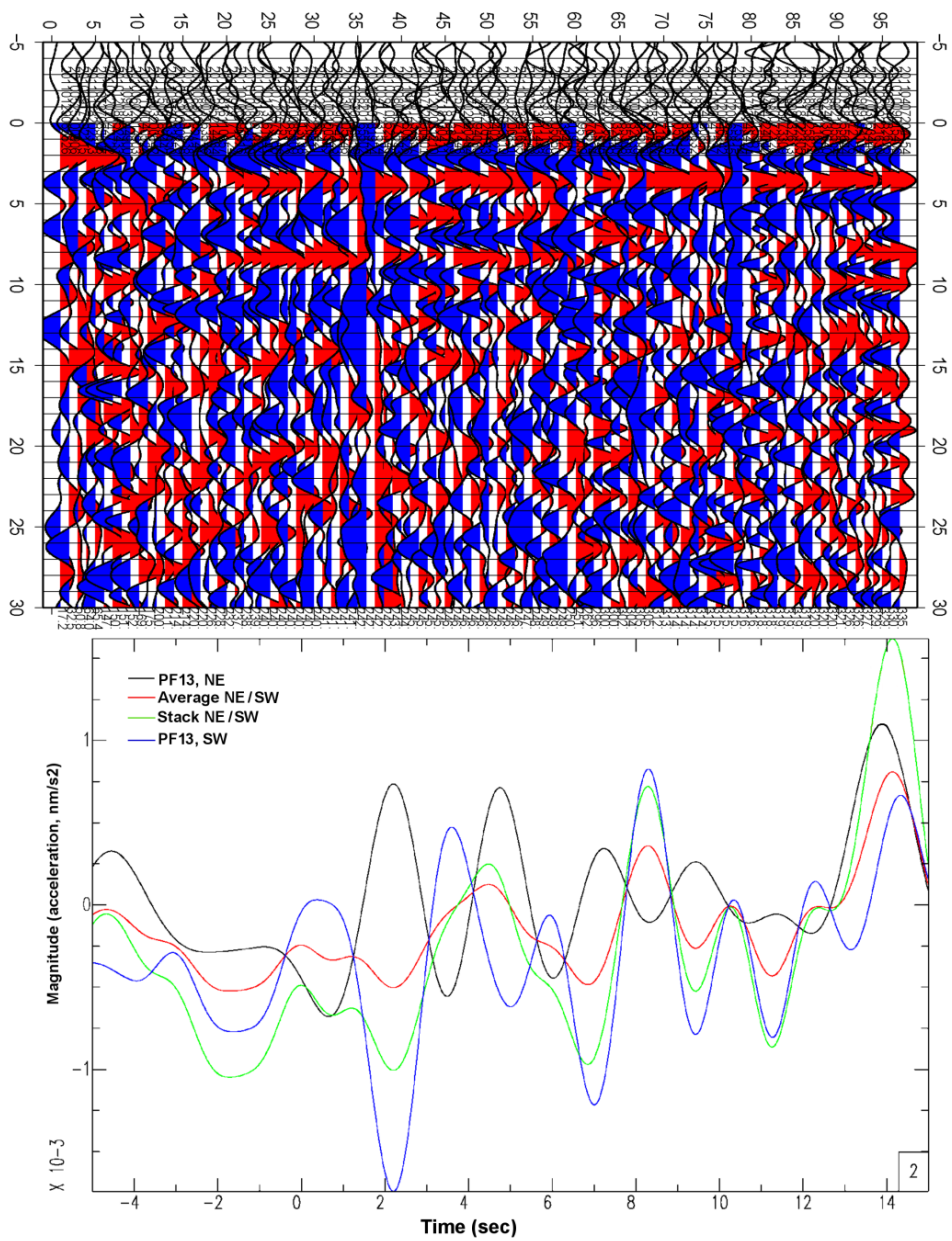


Figure C.11 Transverse RFs for PF13 with traces from the NE and SW directions plotted with their stacks and averages. Note the polarity between the NE and SW trace at about 3 seconds.

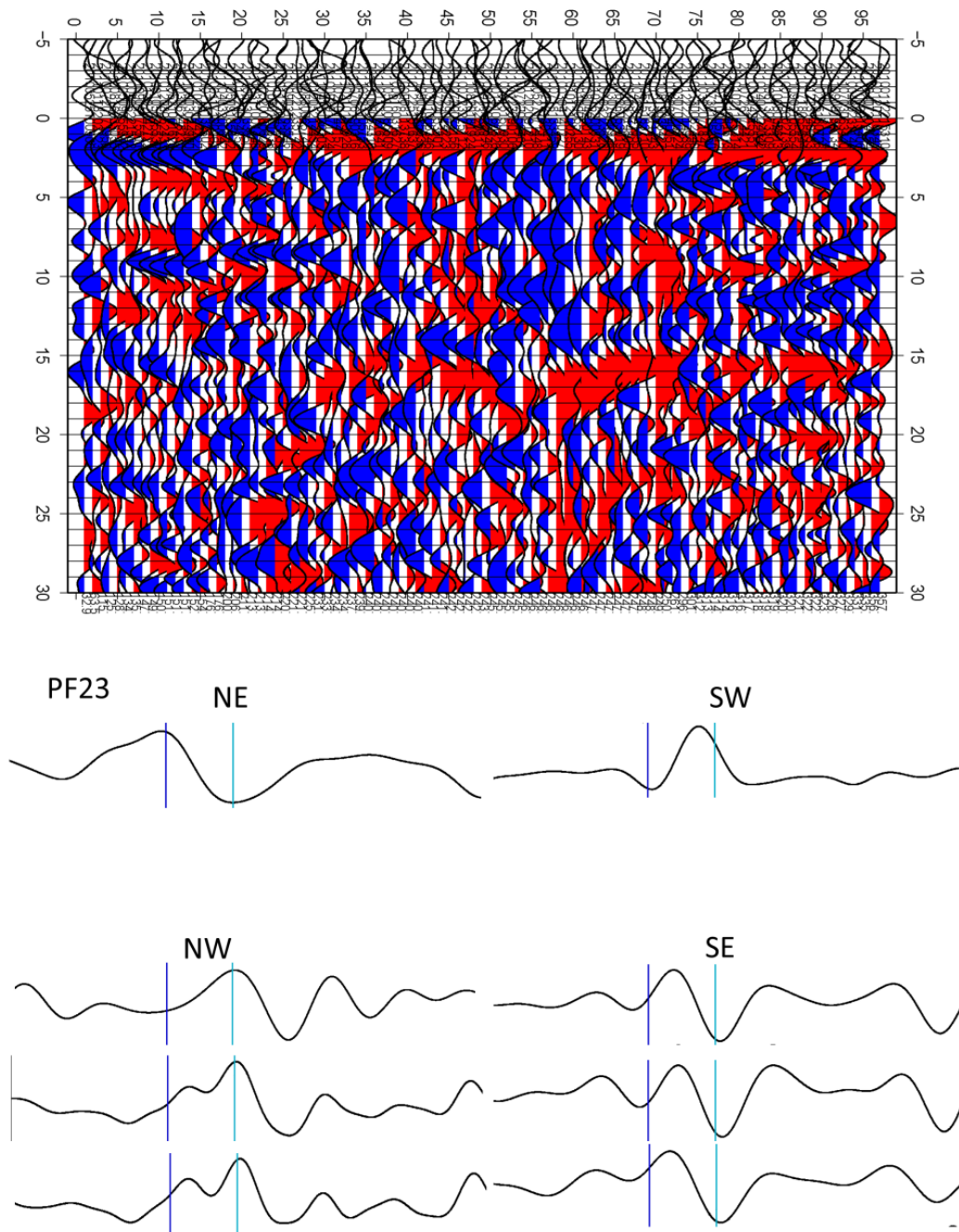


Figure C.12 Transverse RFs for PF23 (Line 2) from the major azimuthal directions.

Notice the polarity differences at about two seconds for the NE compared to SW

directions and NW compared to SE directions.

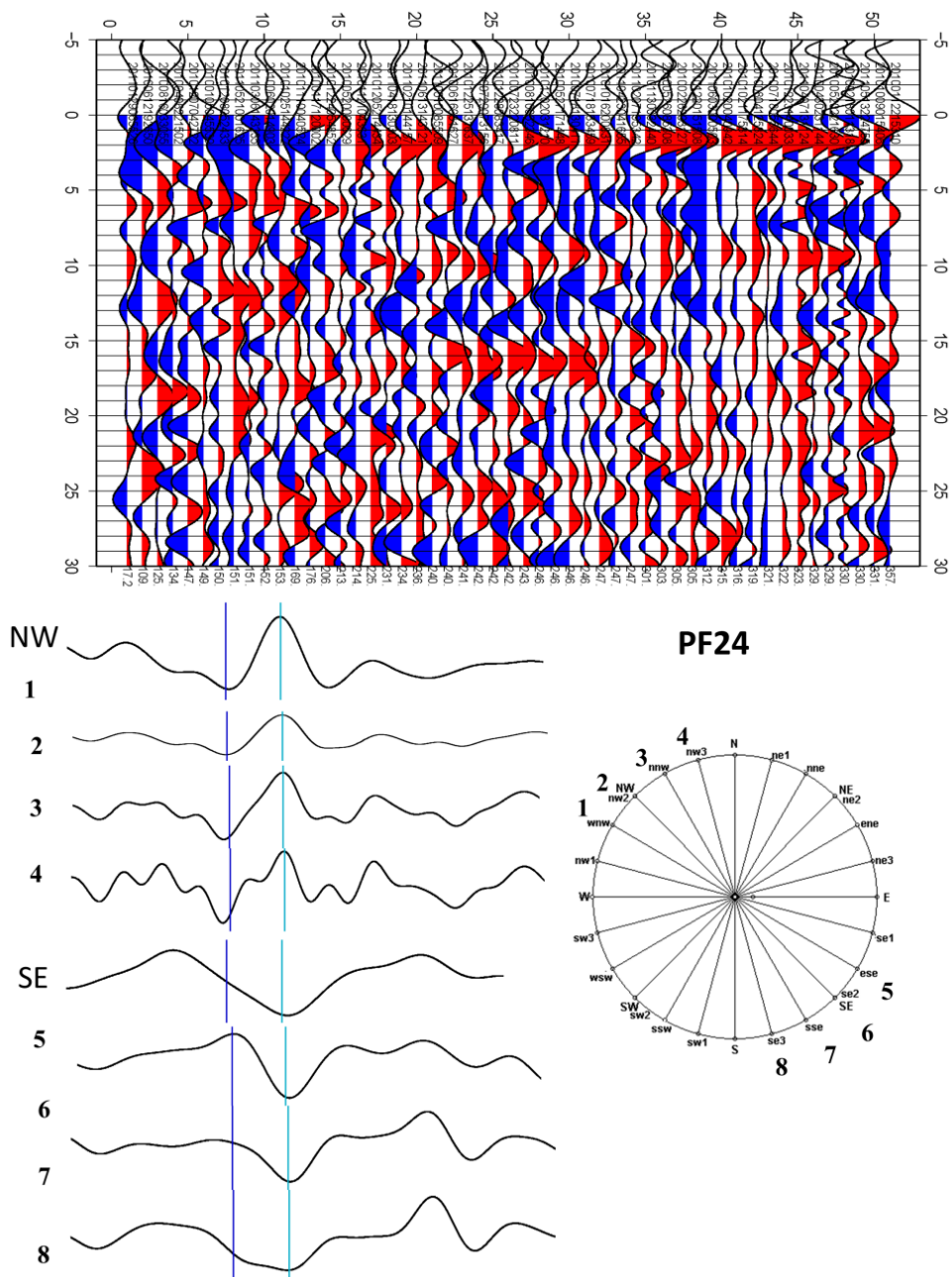


Figure C.13 Transverse RFs for station PF24 (Line 2). The circle shows the central direction that the transverse receiver functions are stacked over. The traces from 180 degrees apart are of opposite polarity at the time of the major arrival (around 2 seconds).

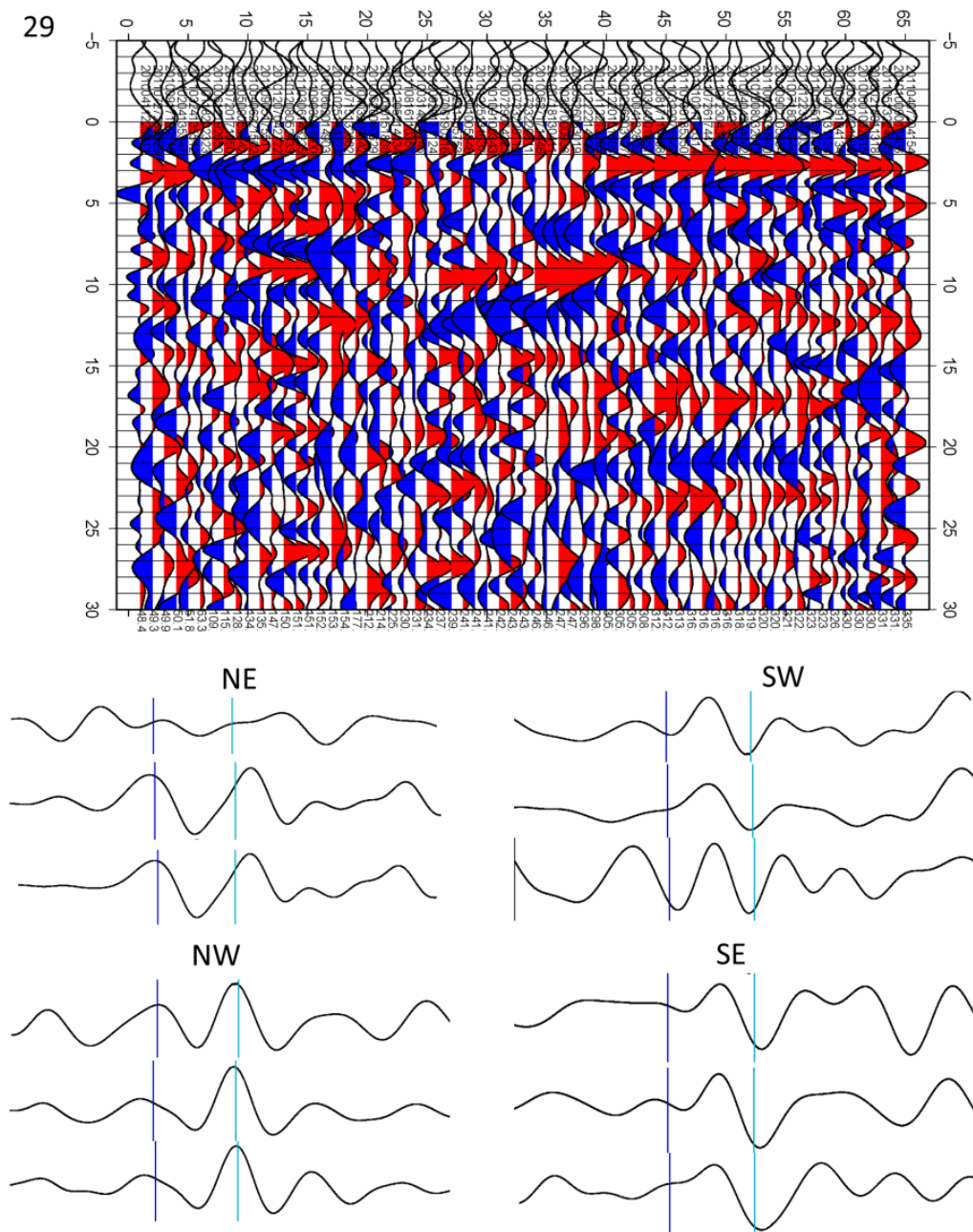


Figure C.14 Transverse RFs for stations PF29 (Line 2) and azimuthal stacks for the major directions. Note the different polarities between directions 180 degrees apart.

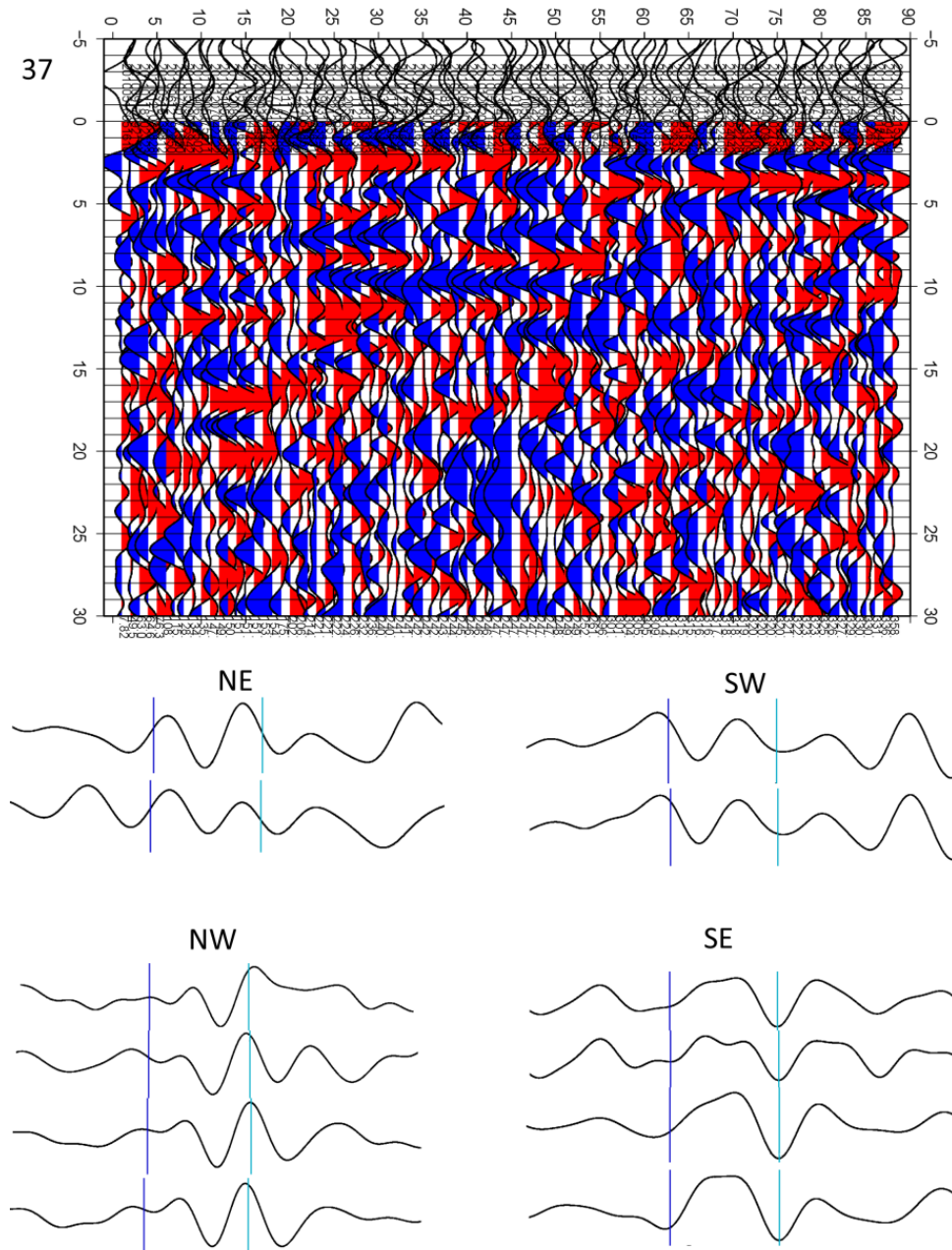


Figure C.15 Transverse RFs for station PF37 (Line 2) and stacks from the major azimuthal directions. Traces are similar for the NE/SW directions but the polarities between the NW and SE directions are opposite for the main arrival (marked by the light blue line) at about 3.5 seconds.

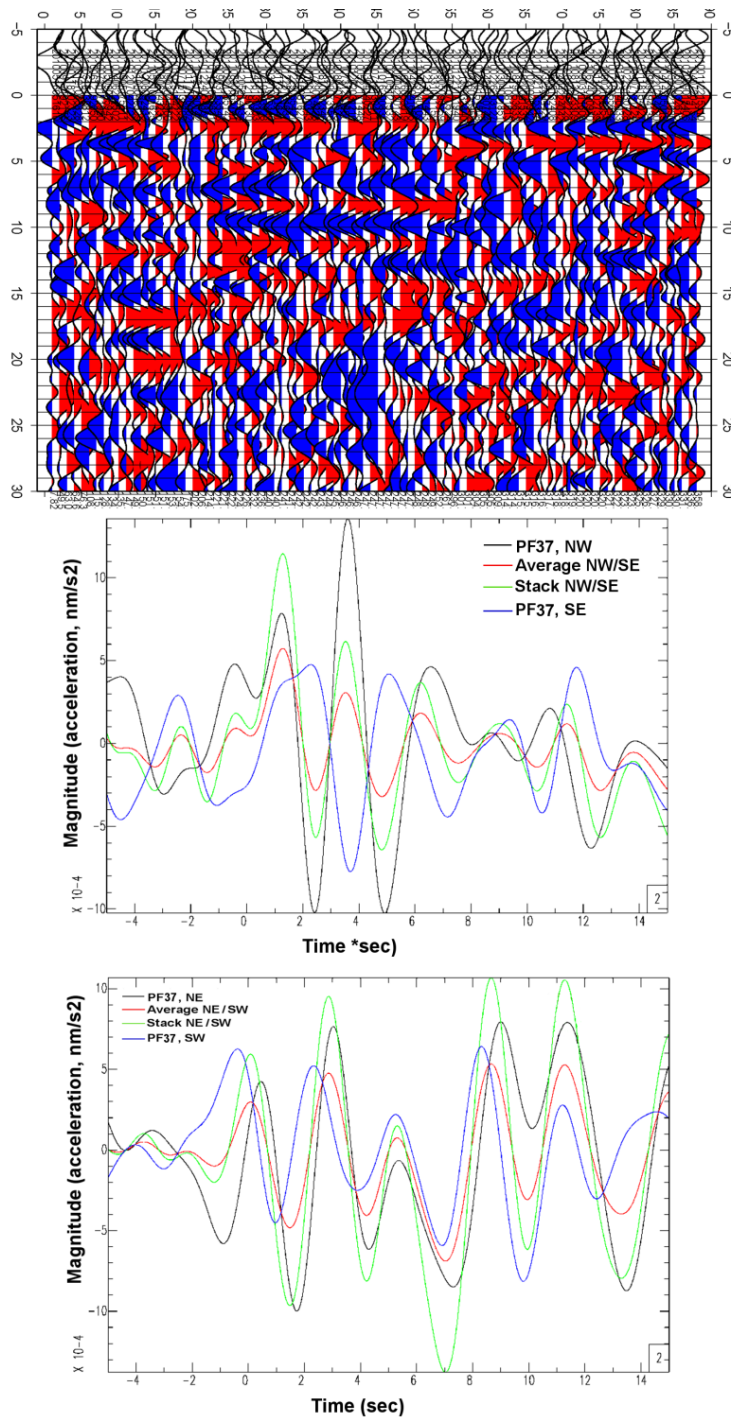


Figure C.16 Similar to figure C.15 but showing the PF37 traces from directions 180 degrees apart along with their stack and average.

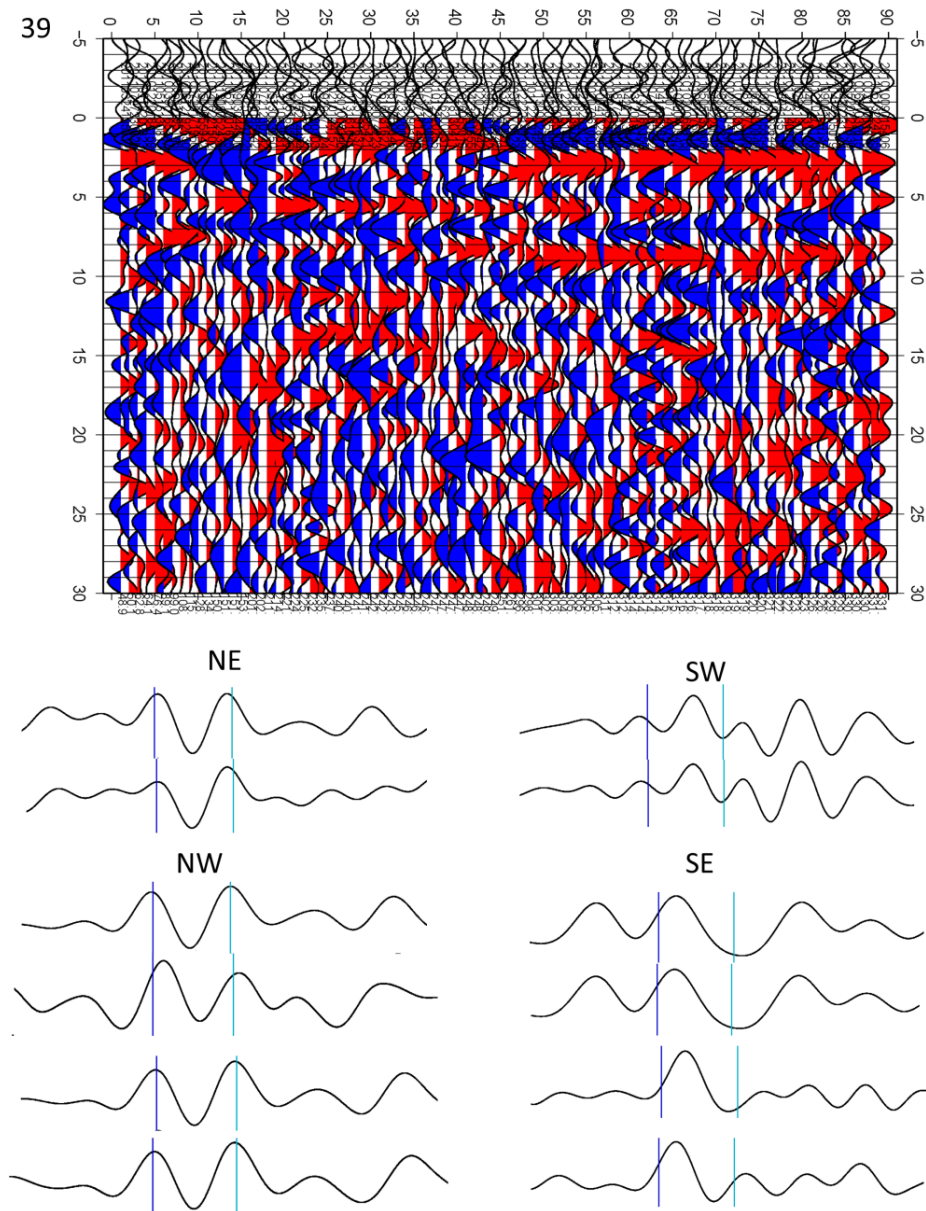


Figure C.17 Transverse RFs for station PF39 (Line 2) and stacked traces from the major azimuthal directions. The largest arrival (marked in light blue) appears to be of opposite polarity for transverse RFs 180 degrees apart in azimuth.

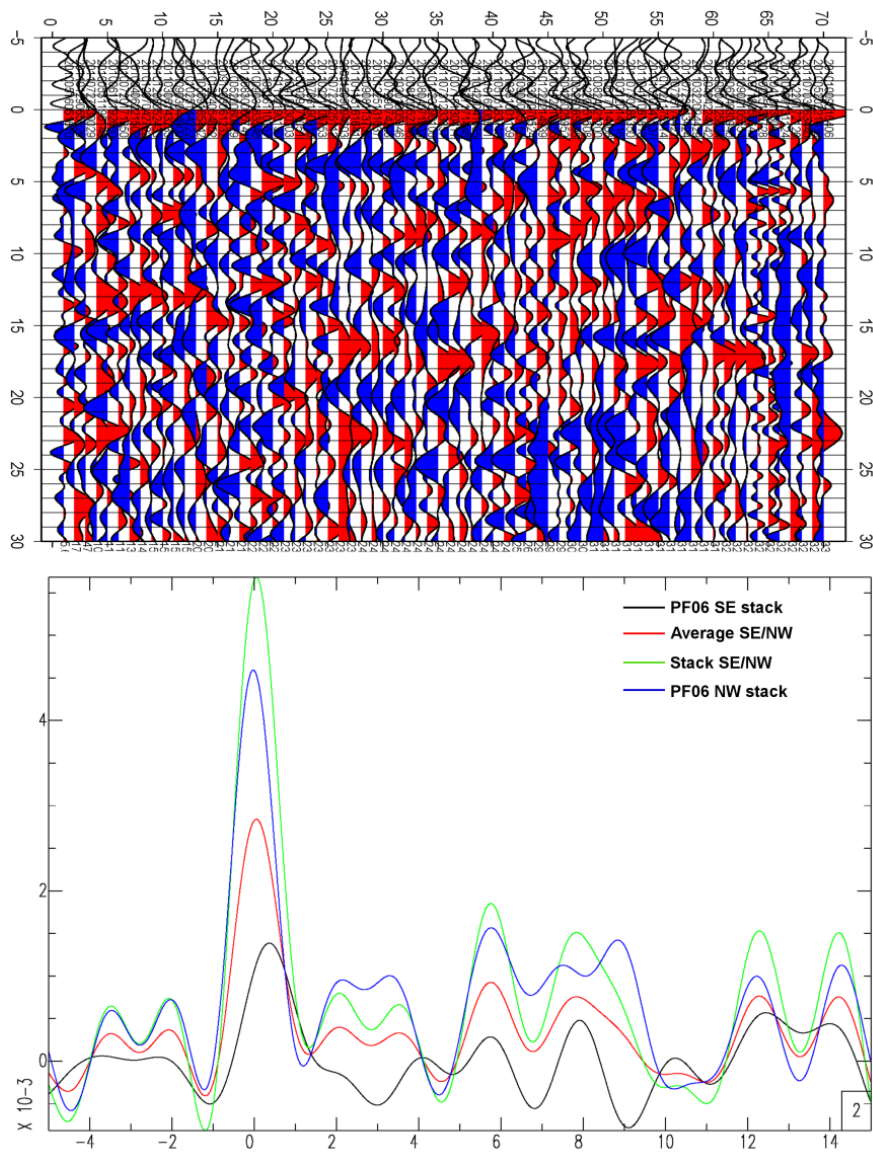


Figure C.18 Transverse RFs for PF06 (Line 2). Traces 180 degrees apart (SE and NW) appear to be in phase in contrast with the nearest station (see figure C.19) and many other stations in the array.

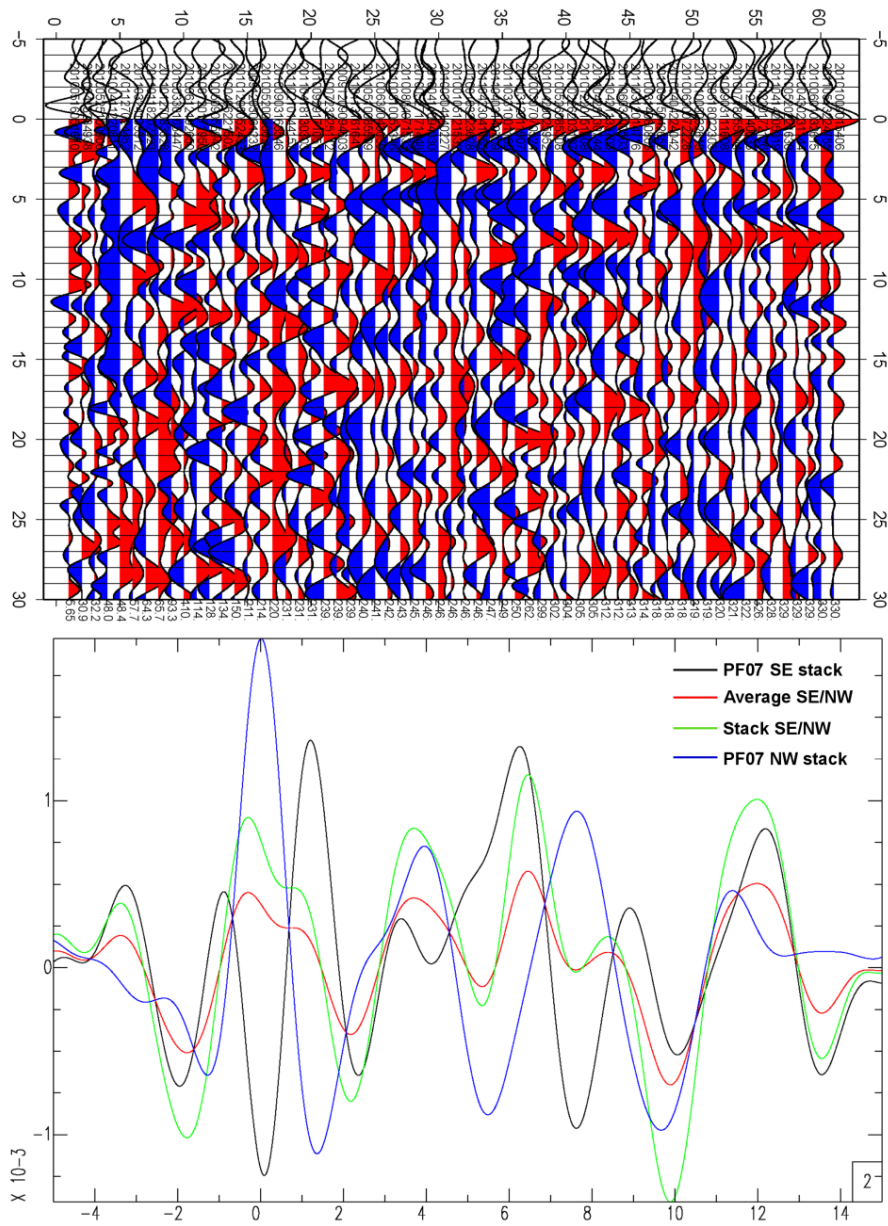


Figure C.19 Transverse RFs for station PF07 (Line 2) along with traces from the SE and NW directions shown with their average and stack. Major arrivals appear to be of opposite polarity.

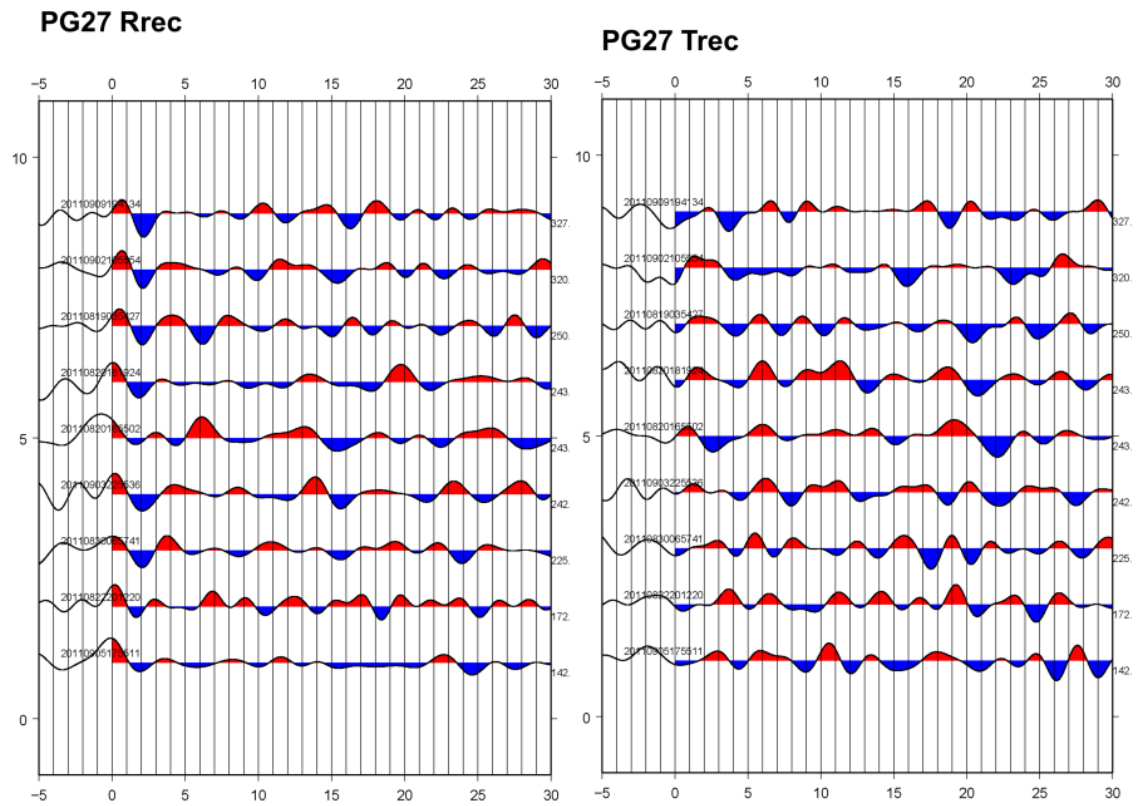


Figure C.20. Comparison of radial and transverse receiver functions for station PG27

(Line 3).

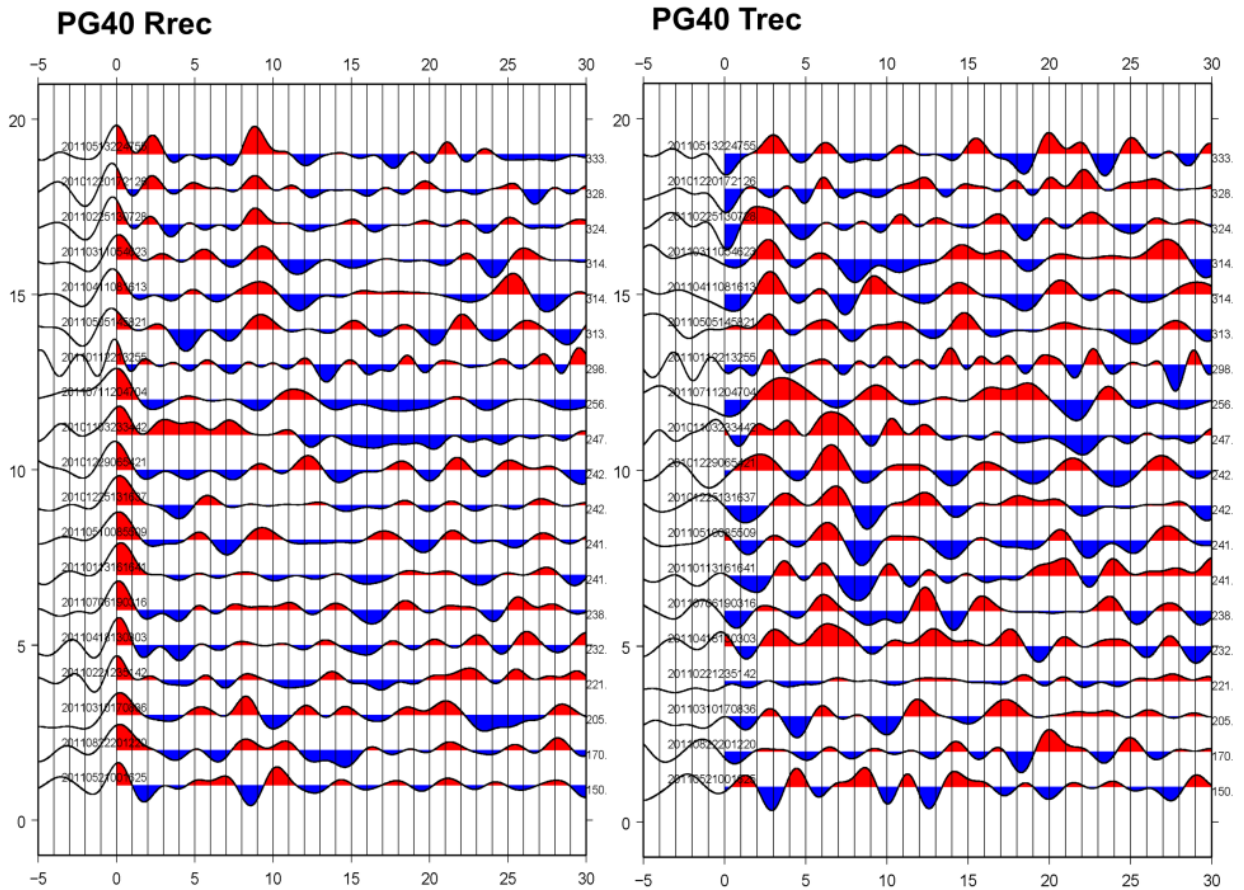


Figure C.21. Radial and transverse RFs for station PG40 (Line 3). Arrivals on the transverse receiver function do not appear to vary by azimuth which may indicate a dip or dipping symmetry axis of anisotropy.

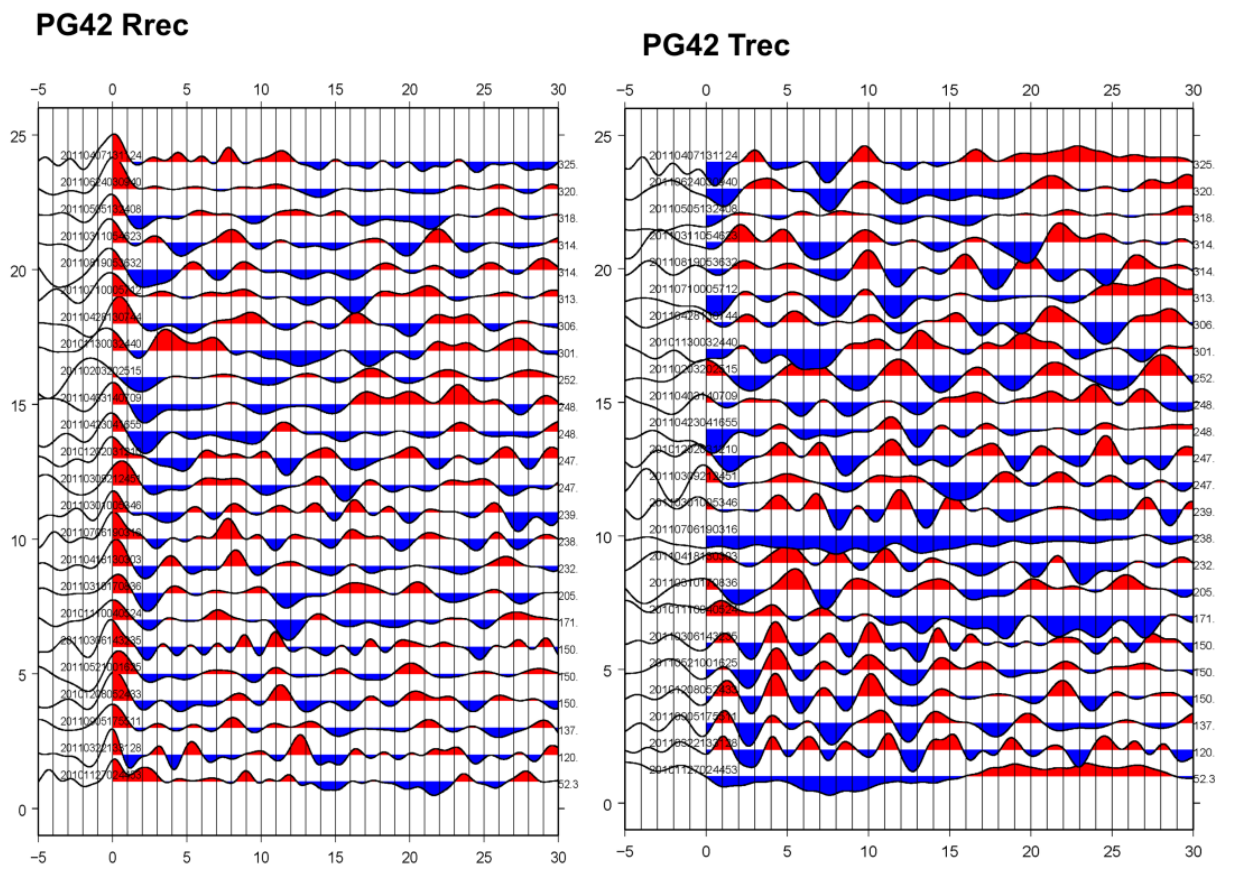


Figure C.22. Radial and transverse receiver functions for station PG42 (Line 3).

11/22/2011, Line 1, bandpassed 2 to 100 sec

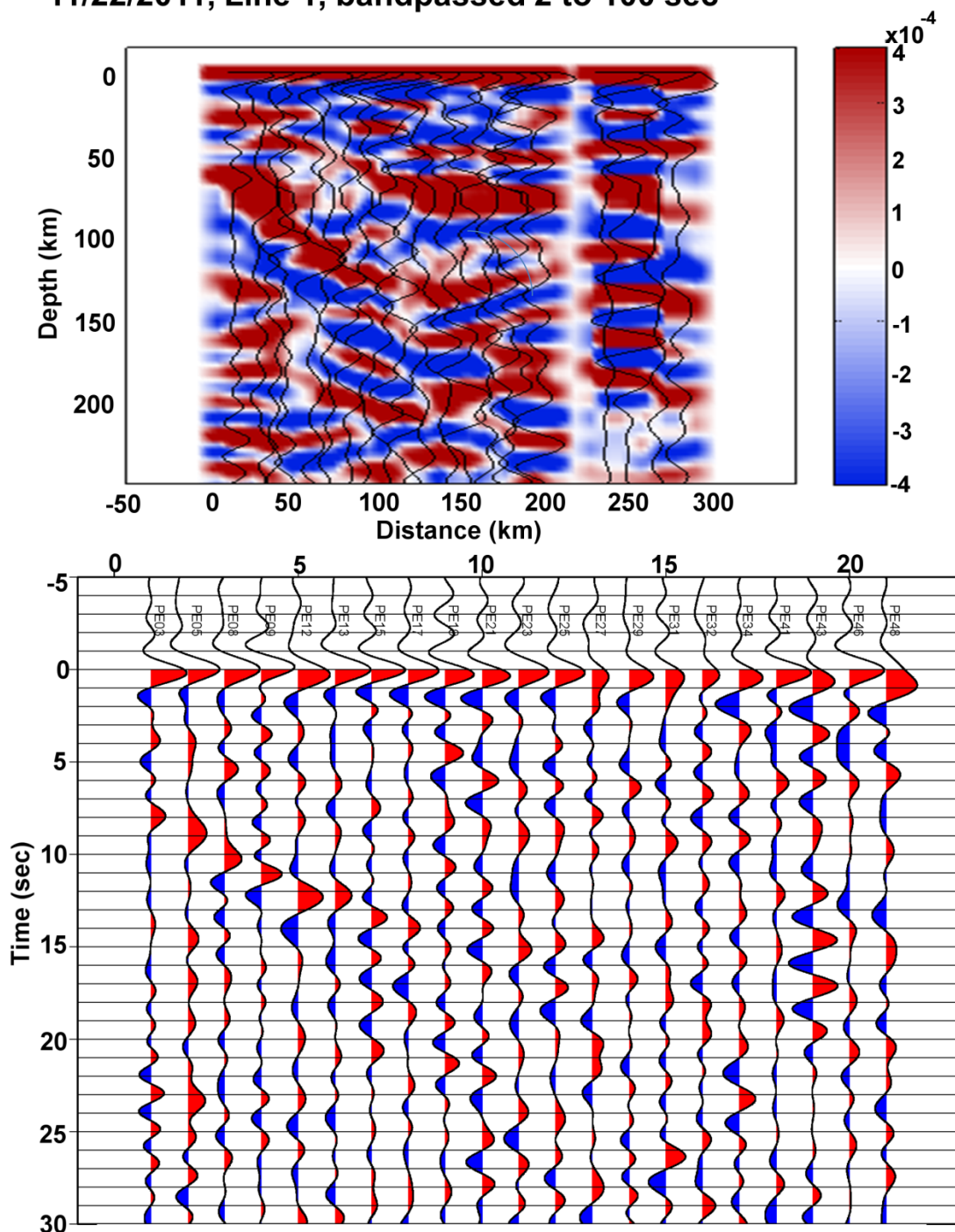


Figure C.23. Same as figure 4.28 but without interpretive lines.

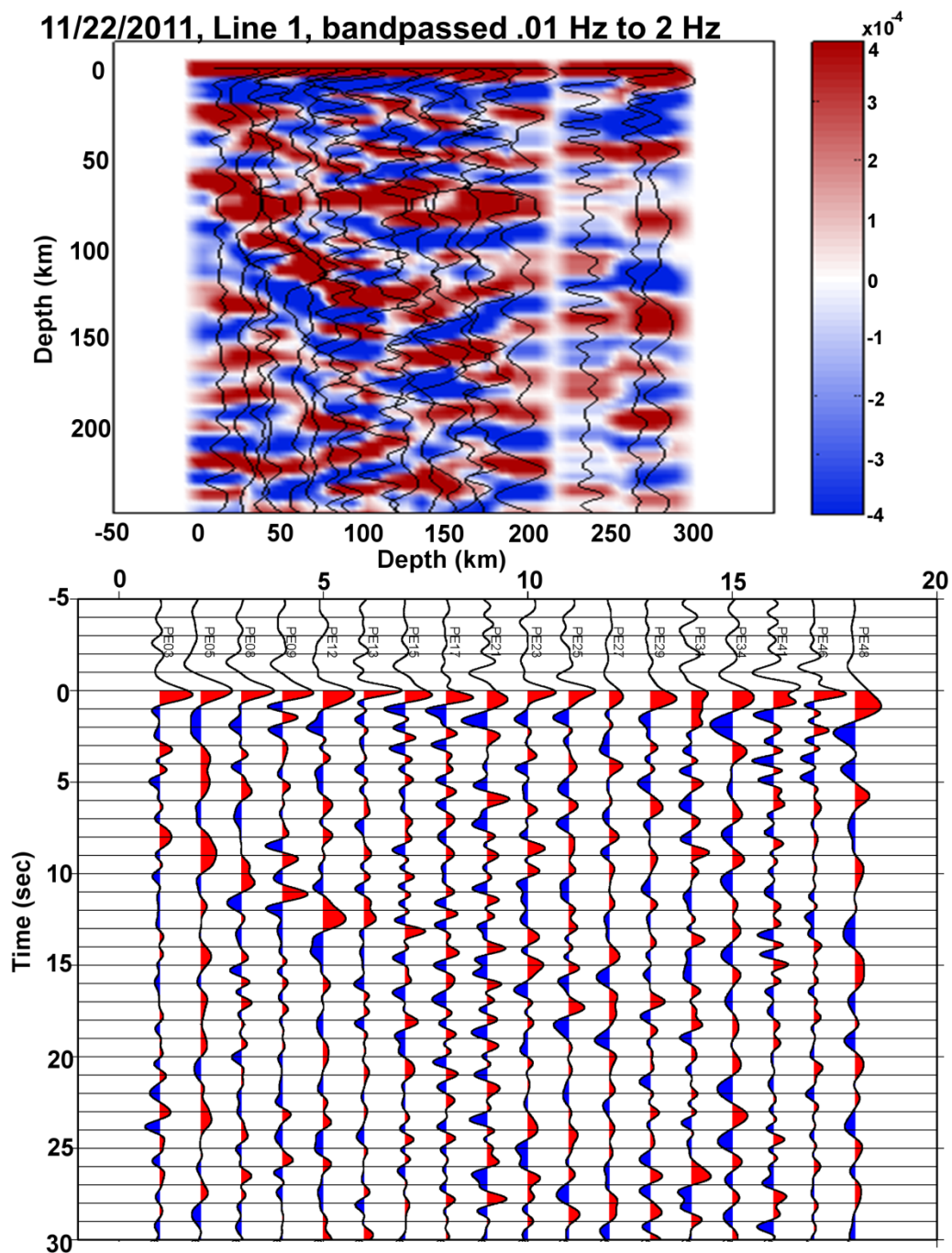


Figure C.24 Local event RF analysis, Line 1, 11/22/2011, 2 Hz bandpass, no interpretive lines (compare with figure 4.29).